Biomedical Physics & Engineering Express

Endorsed by IPEM Institute of Physics and Engineering in Medicine

PAPER

Modeling surface pH measurements of oocytes

To cite this article: A Bocchinfuso *et al* 2022 *Biomed. Phys. Eng. Express* **8** 045006

IOP Publishing Biomed. Phys. Eng. Express 8 (2022) 045006 https://doi.org/10.1088/2057-1976/ac71d0

Biomedical Physics & Engineering Express

PAPER

Modeling surface pH measurements of oocytes

RECEIVED
4 January 2022

REVISED
5 May 2022

ACCEPTED FOR PUBLICATION
20 May 2022

PUBLISHED
3 June 2022

A Bocchinfuso, D Calvetti and E Somersalo*

Department of Mathematics, Applied Mathematics, and Statistics, Case Western Reserve University, 10900 Euclid Avenue, Cleveland, OH 44106, United States of America

* Author to whom any correspondence should be addressed.

E-mail: erkki.somersalo@case.edu

Keywords: cell membrane permeability, gas transport, finite element method, model reduction

Abstract

The transport of gases across cell membranes plays a key role in many different cell functions, from cell respiration to pH control. Mathematical models play a central role in understanding the factors affecting gas transport through membranes, and are the tool needed for testing the novel hypothesis of the preferential crossing through specific gas channels. Since the surface pH of cell membrane is regulated by the transport of gases such as CO_2 and NH_3, inferring the membrane properties can be done indirectly from pH measurements. Numerical simulations based on recent models of the surface pH support the hypothesis that the presence of a measurement device, a liquid-membrane pH sensitive electrode on the cell surface may disturb locally the pH, leading to a systematic bias in the measured values. To take this phenomenon into account, it is necessary to equip the model with a description of the micro-environment created by the pH electrode. In this work we propose a novel, computationally lightweight numerical algorithm to simulate the surface pH data. The effect of different parameters of the model on the output are investigated through a series of numerical experiments with a physical interpretation.

1. Introduction

Gas transport through cell membranes is one of the essential processes supporting life. To understand how central cross-membrane gas transport is, it suffices to follow the pathway of oxygen molecules as they move from the alveoli to erythrocytes, travel with the blood flow, are released, and once they reach the tissue, enter the cells. Once inside the cell, oxygen molecules must cross the mitochondrial outer member to participate in the oxidative phosphorhylation. Carbon dioxide follows a similar pathway in the reverse direction. Traditional models of gas transport through cell membrane, based for the most part on the classical work of Overton [1], assume that gases cross the phospholipid bilayer constituting cell membranes by dissolving into the lipid phase of the membrane and diffusing along a concentration gradient. The discovery of cell membranes that are practically impermeable to gases such as ammonia and carbon dioxide [2] required a revision of this diffusion model, and pointed to the need for a better explanation for the mechanism of gas transport through membranes. Further studies on this topic [3] provided some evidence that certain proteins bound to the membrane, most notably different isoforms of aquaporins (AQP) and rhesus proteins (Rh), can provide plausible pathways for gases. For a comprehensive overview of the history and current understanding of the gas transport through membranes, we refer to [4].

Another important function where gas transport plays a key role is pH regulation. Several vital cell functions require that the intra- and extracellular pH remain within a range of normal values. One of the ways in which cells can control the acid-base balance is the transport of acids and bases across the membrane. The membrane permeability to protons H^+ and ions such as bicarbonate HCO_3^- may be too limited for effective pH control, making shuttle mechanisms based on gas transport an important factor of pH regulation: see figure 1 for a schematic illustration.

Because of the important role of gas transport across cell membrane for the pH control, it has been suggested that pH measurements could be used to infer indirectly on the cell membrane permeability to gases [5]: If the pH on the outer surface of the cell membrane and inside the cell depends on membrane permeability to gases,

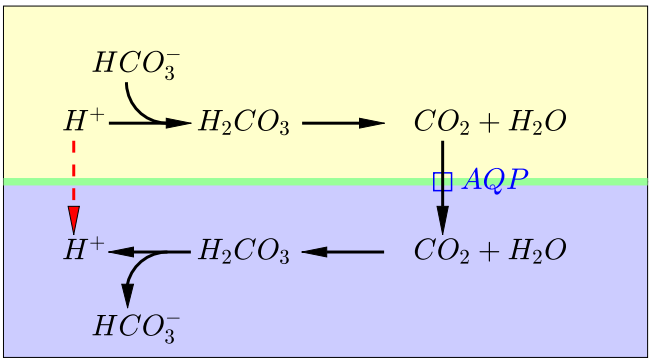

Figure 1. Shuttle mechanism for the virtual passage of a proton through cell membrane: The proton H^+ outside the cell (yellow) associates with bicarbonate HCO_3^- to form carbonic acid H_2CO_3, which dissociates into CO_2 and water. The carbon dioxide concentration gradient across the membrane causes the passage of the gas through the membrane, and a reverse reaction inside the cell (purple) frees a proton, lowering pH as if the proton had crossed the membrane.

the estimation of the permeability based on pH measurements requires the solution of an inverse problem that links the quantities through a mathematical model. In turn, the solution of the inverse problem requires a computational forward model that takes into account all pertinent factors contributing to the data. Mathematical models for gas transport through cell membranes of different complexity have been proposed in the literature, see, e.g. [6]. The basis for a spatio-temporal distributed reaction-diffusion model taking into account the geometry, possible buffers and distribution of carbonic anhydrase was laid in [7] and the model predictions were compared with experimental data on the oocytes of African clawed frog *Xenopus laevis* [8]. This spherical cell, ideal for physiological studies because of its large size, approximately 1.3mm in diameter, allows experimental manipulations such as measurements of surface pH, and it is an outstanding system for the heterologous expression of the membrane proteins encoded by injection of foreign RNA [9].

In the experimental setup, an oocyte expressing membrane proteins of interest is exposed to elevated CO_2 concentration by placing it in a liquid whose composition can be externally controlled. The tip of a liquid-membrane pH-sensitive electrode, about 10 μm in diameter, is placed on the cell membrane and the time trace of the surface pH, denoted by $pH_S(t)$, is recorded. Because of the spherical symmetry of the oocyte, the reaction-diffusion model in spherical coordinates reduces to a system of one space dimension that is relatively straightforward to time integrate numerically. In [7], using a computational scheme based on a finite difference discretization in the radial coordinate, it was demonstrated that the model correctly describes the qualitative behavior of the surface and interior pH. The dynamical range and the time constants of the surface pH curve, however, did not match the measured values, even when a moderate enhancement by the enzyme carbonic anhydrase (CA) was added to the model, suggesting that some important details might be missing. The hypothesis that the measurement device itself could affect the outcome by creating a microenvironment under the pH electrode was formulated and tested with a computational model in [10]. In that contribution it was shown that a model for partial clamping, created by pushing the electrode tip against the membrane, was able to produce a dynamic behavior in line with the measured surface pH. The computational model in [10], which is based on a detailed finite element method (FEM) discretization of the domain around the electrode tip, leads to a large time-dependent system with hundreds of thousands degrees of freedom, and requires special implicit/explicit iintegrators to address the singular perturbation problem arising from the multiscale nature of the problem in the time domain.

The goal of the current contribution is to address the computational challenges of the numerical simulations aimed at studying the effect of the electrode on pH. Regardless of whether optimization-based or statistical sampling-based methods are used to address the inverse problem of retrieving the membrane properties from the pH data, the forward model needs to be solved repeatedly. Unfortunately the model with a detailed description of the electrode tip is too slow for these purposes, each forward solve requiring several hours of computer time, highlighting the need for a proxy model capable of approximating the detailed model output with reasonable accuracy at a fraction of the computing time, while depending on parameters amenable to a clear physical interpretation. In this article we propose such model and we demonstrate that it produces quantitatively correct pH dynamics on the outer surface of the cell membrane and inside the cell. The convenience of having a nimble reduced model is demonstrated in this article by investigating systematically the effect of different parameters on the predicted output, a task that with the detailed FEM model would be prohibitively time consuming. The model predictions are compared to measured values reported in the literature. We also show that the approximate model can be used to design a non-linear

gain functional that represents the measurement device, mapping the free membrane concentrations to the measured surface pH, thus breaking the proposed algorithm into two conceptually separate parts.

2. An overview of the underlying reaction-diffusion model

We assume that a spherical oocyte of radius R is placed in an infinite liquid environment, with the origin of the coordinate system coinciding with its center. A reaction-diffusion equation is set up for concentration distributions of carbon dioxide (CO_2), bicarbonate (HCO_3^-), carbonic acid (H_2CO_3) and protons (H^+), and possible pH buffers inside and outside the cell membrane, coupled through physiological parameters such as membrane permeability. Consider the following set of chemical reactions taking place both in the extracellular liquid and in the cytoplasm,

$$CO_2 + H_2O \underset{k_{-1}}{\overset{k_1}{\rightleftharpoons}} H_2CO_3, \tag{1}$$

$$H_2CO_3 \underset{k_{-2}}{\overset{k_2}{\rightleftharpoons}} HCO_3^- + H^+, \tag{2}$$

$$HA_\ell \underset{k_{-(2+\ell)}}{\overset{k_{2+\ell}}{\rightleftharpoons}} A_\ell^- + H^+, \quad 1 \leqslant \ell \leqslant L, \tag{3}$$

where A_ℓ^- is a buffer different from the bicarbonate HCO_3^-. For simplicity we only consider the case of one non-specified buffer, that is, $L = 1$, so that the total number of chemical species is $N = 4 + 2L = 6$. We use the following numbering for the concentrations,

$$u_1 = [CO_2], \quad u_2 = [H_2CO_3], \quad u_3 = [HCO_3^-], \\ u_4 = [H^+], \quad u_5 = [HA], \quad u_6 = [A^-]. \tag{4}$$

The concentrations are functions of the position $x \in \mathbb{R}^3$ and time $t \geqslant 0$, that is $u_\nu^\pm = u_\nu^\pm(x, t)$, where the superscript $\pm$ specifies whether we refer to values outside $(+)$ or inside $(-)$ of the cell membrane. The concentrations satisfy the coupled system of reaction-diffusion equations,

$$\frac{\partial u_\nu^\pm}{\partial t} = \nabla \cdot (\boldsymbol{\kappa}_\nu^\pm \nabla u_\nu^\pm) + \sum_{\mu=1}^{N} S_{\nu\mu} \Phi_\mu^\pm, \quad 1 \leqslant \nu \leqslant N, \tag{5}$$

where $\boldsymbol{\kappa}_\nu^\pm \in \mathbb{R}^{3\times 3}$ is the diffusion tensor of the νth species inside or outside the membrane. The coefficients $S_{\nu\mu}$ are the components of the stoichiometric matrix, and $\Phi_\mu^\pm$ is the flux of the μth reaction, modeled by using mass action laws, see appendix A for details. The inside and outside reaction-diffusion models are coupled through the flux of CO_2 through the membrane. In the lack of a better model, in [7], we resorted to a Robin boundary condition based on Fick's law,

$$n \cdot \boldsymbol{\kappa} \nabla u_1^+ |_{\Gamma_m} = \lambda (u_1^+ - u_1^-)|_{\Gamma_m} = n \cdot \boldsymbol{\kappa} \nabla u_1^- |_{\Gamma_m}, \tag{6}$$

where Γ_m is the cell membrane, n is the unit normal of the membrane pointing in the exterior domain, and $\lambda > 0$ is the membrane permeability, which is assumed to be constant. In the light of experimental evidence, it is reasonable to assume that the membrane layer is practically impermeable to H^+ [11] and bicarbonate HCO_3^- [12], and therefore the flux of other substances through the membrane is ignored in the model. For the initial condition, we assume that the concentrations both inside and outside the cell are in chemical equilibrium, and that the exterior concentration of CO_2 is higher than inside,

$$u_1^+(x, 0) = u_{1,0}^+ > u_{1,0}^- = u_1^-(x', 0), \quad |x| > R > |x'|. \tag{7}$$

The forward problem is to compute the time trace of the exterior surface pH for given λ,

$$\mathrm{pH}_S(t) = -\log_{10} u^+(x, t)|_{|x|=R+}, \tag{8}$$

the concentration given in moles per liter. The inverse problem that is beyond the scope of this article, would be to estimate the permeability from observed $\mathrm{pH}_S(t)$.

Because of the spherical symmetry, if we write the problem in spherical coordinates (r, θ, φ) the model (5) reduces to a one-dimensional radial reaction-diffusion model,

$$\frac{\partial u_\nu^\pm}{\partial t} = \frac{1}{r^2}\frac{\partial}{\partial r}\left(\kappa_\nu^\pm r^2 \frac{\partial u_\nu^\pm}{\partial r}\right) + \sum_{\mu=1}^{N} S_{\nu\mu}\Phi_\mu^\pm, \tag{9}$$

which can be semidiscretized and solved by the method of lines. Above, the scalar $\kappa_\nu^\pm$ is the coefficient of the radial diffusion. In [7], the semidiscretization was done by finite differences, while here we use the finite element method (FEM); the details of the FEM can be found in appendix B.

The radial model reproduces correctly the qualitative behavior of the surface pH: At the beginning of the experiment, a strong influx of CO_2 into the cell causes a decrease of the intracellular pH with a concomitant increase of the pH on the outside. Over time, as the CO_2 concentration inside the cell increases, the CO_2 influx slows down, while its concentration outside the membrane is replenished by diffusion. This causes the surface pH curve to first peak and then to decrease, eventually returning asymptotically to the original equilibrium value. However, the peak value of pH_S computed by the model is significantly lower than the measured value, and the time constant of the pH dynamics does not correspond to the data, reported, e.g., in [8]. A slight improvement was obtained by adding to the model the enzyme carbonic anhydrase (CA) which is known to be present in cytosol and on the cell membrane, albeit in unknown quantities. The effect of CA is to speed up the reactions (1). The presence of CA is included in the model by modifying in the reaction fluxes Φ_1 and Φ_2 corresponding to (1), see appendix A,

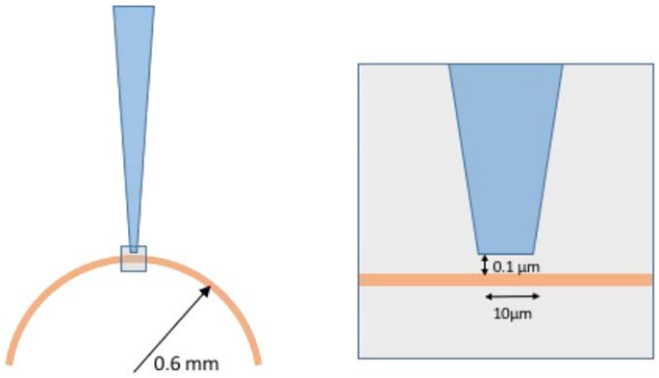

Figure 2. Geometry of the electrode tip model. The rectangular gray area on the left is approximated by assuming that the cell membrane is planar as shown in the right panel. In the FEM model, the boundary values around the computational domain are obtained from the radial model.

$$\Phi_1^-(r,\,t) = Ak_1u_1^-(r,\,t), \quad \Phi_1^+(r,\,t) = \begin{cases} Ak_1u_1^+(r,\,t), & R < r \leqslant R+\delta, \\ k_1u_1^+(r,\,t), & r > R+\delta, \end{cases} \tag{10}$$

and, similarly for the reverse reaction,

$$\Phi_2^-(r,\,t) = Ak_{-1}u_2^-(r,\,t), \quad \Phi_2^+(r,\,t) = \begin{cases} Ak_{-1}u_2^+(r,\,t), & R < r \leqslant R+\delta, \\ k_{-1}u_2^+(r,\,t), & r > R+\delta, \end{cases} \tag{11}$$

Here $A > 1$ is the enhancement factor caused by the CA, and $\delta > 0$ is a parameter defining the thin boundary layer beyond which the enzyme is not present. The addition of CA in moderate amounts to the model increases the peak value of the surface pH, but the new value is still below the measured one. We refer to [7] for a detailed discussion of the values of the factor A and its effect on pH dynamics.

2.1. Electrode tip microenvironment

The numerical simulations in [10] support the hypothesis that the pH electrode tip itself may significantly affect the outcome of the measurement, as the dynamics of the pH concentration curve computed by the model corresponds well to the measured data. When the tip is pushed against the cell membrane, a pocket under the tip forms, with limited access of the substances from the exterior domain to this pocket. Since the readings of the electrode come from the microenvironment, they may not correspond to the pH on the free membrane. In the numerical simulations in [10], the computational domain of the reaction-diffusion model was a cylindrical region around the electrode tip, discretized using a finite element mesh with angular symmetry around the electrode axis, see figure 2. The values along the cylinder exterior boundaries were computed by using the radial model discussed above, and the access to the space under the tip was limited by reducing the diffusion coefficient under the rim of the electrode tip by a multiplicative factor, $\kappa \to e^{-q}\kappa$. The parameter $q > 0$ was referred to as the *quench parameter*.

While the detailed electrode tip model satisfactorily explains the discrepancy between the simulated surface pH values and the measurements, it depends on model parameters that effectively are impossible to measure, such as the thickness of the clamped pocket and the quenching parameter, and its high computational complexity makes it unsuited for inversion algorithms. In fact, because of the combination of hundreds of thousands degrees of freedom and the need to address the singular perturbation issues related to the temporal multiscale nature of the problem, each single forward solve requires hours of computing time. In the following discussion, a simple approximate reduced model is developed.

2.2. Lumped compartment model

In this subsection we derive a lower complexity model that is able to account for the presence of the electrode tip that partially clamps the pocket between the tip and the cell membrane dimple created by it. We assume that a spherical oocyte of radius $R > 0$ is placed in an infinite liquid that originally is in constant chemical equilibrium. The dynamics of the concentrations, in the absence of the electrode, are described by a radial reaction-diffusion model similar to the one in [7]. We modify the model to account for the presence of the electrode tip against the outer membrane of the oocyte by locally perturbing the spherical model near the location of the electrode tip. More specifically, let $P > 0$ be the radius of the electrode tip, which we assume to be circular, and let $h > 0$ be the distance of the tip from the membrane, with the axis of the electrode normal to the membrane. While the membrane in reality is originally close to spherical, and in the presence of the electrode pushed agains it the spherical shape may be slightly perturbed, we assume here for simplicity that locally, the membrane can be approximated by a plane parallel to the electrode tip. We denote by Ω the pillbox domain between the tip and the electrode, and by $|\Omega|$ its volume,

$$|\Omega| = \pi P^2 h. \tag{12}$$

We denote by u_ν^0 the concentrations in Ω, $1 \leqslant \nu \leqslant 6 = N$, satisfying the reaction-diffusion equations

$$\frac{\partial u_\nu^0}{\partial t} = \nabla \cdot \boldsymbol{\kappa}_\nu^0 \nabla u_\nu^0 + \sum_{\mu=1}^{N} S_{\nu\mu} \Phi_\mu^0. \tag{13}$$

Let $\overline{u}_\nu^0$ be the mean concentration of νth substance over Ω, defined as

$$\overline{u}_\nu^0 = \frac{1}{|\Omega|} \int_\Omega u_\nu^0 dx.$$

Averaging equation (13) over Ω leads to an ordinary differential equation,

$$\frac{d\overline{u}_\nu^0}{dt} = \frac{1}{|\Omega|} \int_\Omega \nabla \cdot \boldsymbol{\kappa}_\nu \nabla u_\nu^0 dx + \sum_{\mu=1}^{N} S_{\nu\mu} \overline{\Phi}_\mu^0,$$

where $\overline{\Phi}_\mu^0$ is the average of the μth reaction flux to be discussed later. To simplify the integral term, we denote by B the circular membrane patch under Ω, by B_h the circular electrode tip above Ω, and by S_h the cylindrical peripheral surface of Ω, and use cylindrical coordinates (ρ, θ, z) with the axis of symmetry normal to the cell membrane coinciding with the electrode axis, with $z < 0$ corresponding to the interior of the cell. Integrating by parts and assuming that there is no flux into the electrode,

$$\int_\Omega \nabla \cdot \boldsymbol{\kappa}_\nu^0 \nabla u_\nu^0 dx = \left(\int_B + \int_{B_h} + \int_{S_h} \right) n \cdot \boldsymbol{\kappa}_\nu^0 \nabla u_\nu^0 dS \tag{14}$$

$$= - \int_B e_z \cdot \boldsymbol{\kappa}_\nu^0 \nabla u_\nu^0 \Big|_{z=0} dS + \int_{S_h} e_\rho \cdot \boldsymbol{\kappa}_\nu^0 \nabla u_\nu^0 \Big|_{\rho=P} dS, \tag{15}$$

where e_ρ and e_z are the coordinate unit normal vectors. We assume that the cell membrane is permeable only to carbon dioxide, implying that we may write

$$\int_B e_z \cdot \boldsymbol{\kappa}_\nu^0 \nabla u_\nu^0 \Big|_{z=0} dS = 0, \quad 2 \leqslant \nu \leqslant N. \tag{16}$$

For carbon dioxide, we use the model similar to (6), and by approximating the concentration of u_1^0 at the membrane boundary by $\overline{u}_1^0$, we write

$$\int_B e_z \cdot \boldsymbol{\kappa}_1^0 \nabla u_\nu^0 \Big|_{z=0} dS \approx \lambda \pi P^2 (\overline{u}_1^0 - u_1^-|_{\Gamma_m}), \tag{17}$$

where u_1^- is the concentration inside the cell at the membrane boundary. Along the cylindrical peripheral surface S_h, the integral corresponds to the flux across S_h. We assume that the flux is driven by the concentration gradient across S_h, and write an approximate model

$$\int_{S_h} e_\rho \cdot \boldsymbol{\kappa}_\nu^0 \nabla u_\nu^0 \Big|_{\rho=P} dS \approx 2\gamma\pi P h (u_\nu^+|_{\Gamma_m} - \overline{u}_\nu^0), \quad 1 \leqslant \nu \leqslant N, \tag{18}$$

where we implicitly assumed that h is small, and on the peripheral surface, we use the fact that the approximately radially symmetric exterior concentration u_ν^+ is well approximated by the boundary value at the membrane. Here, $\gamma > 0$ is a parameter modeling the limited mobility of substances between the free liquid space and the compartment Ω partly clamped by the rim of he electrode tip pushing against the membrane.

Combining (16)–(18), we arrive at the ordinary differential equation model for the average concentrations under the electrode tip,

$$\frac{d\overline{u}_\nu^0}{dt} = -\delta_{\nu 1} \frac{\lambda}{h} (\overline{u}_\nu^0 - u_\nu^-|_{\Gamma_m}) + \frac{2\gamma}{P} \left(u_\nu^+|_{\Gamma_m} - \overline{u}_\nu^0 \right) + \sum_{\mu=1}^{N} S_{\nu\mu} \overline{\Phi}_\mu^0, \tag{19}$$

where $\delta_{\nu 1}$ is the Kronecker symbol.

The average reaction fluxes $\overline{\Phi}_\mu^0$ are approximated by writing the standard mass balance equations in terms of the average concentrations. To address the fact that at least a part of the domain under the electrode tip is affected by the carbonic anhydrase attached to the cell membrane, while part may be unaffected by it, we modify the hydration/dehydration reactions fluxes of carbon dioxide by writing

$$\overline{\Phi}_1^0 = A^0 k_1 \overline{u}_1^0, \quad \overline{\Phi}_2^0 = A^0 k_{-1} \overline{u}_2^0, \tag{20}$$

where A^0 is the parameter accounting for the CA acceleration, with $1 \leqslant A^0 \leqslant A$.

We may now summarize the lumped electrode model: Find the functions $(u_\nu^-(r, t), u_\nu^+(r, t), \overline{u}_\nu^0(t))$ satisfying the equations (9) and (19), with the coupling condition (6), the initial values

$$u_\nu^+(x, 0) = u_\nu^0(0) = u_{\nu,0}^+, \quad u_\nu^-(x, 0) = u_{\nu,0}^-, \quad 1 \leqslant \nu \leqslant N, \tag{21}$$

and the asymptotic value

$$\lim_{r \to \infty} u_\nu^+(r, t) = u_{\nu,0}^+, \quad 1 \leqslant \nu \leqslant N, \tag{22}$$

where the limiting values coincide with the exterior initial values. The formula for the surface pH function is

$$\mathrm{pH}_S(t) = -\log_{10} \overline{u}_4^0(t), \quad t \geqslant 0. \tag{23}$$

Observe that although the equations (9) and (19) are coupled, it is reasonable to assume that, due to the small size of the compartment Ω, the effect of the solution $\overline{u}_\nu^0$ on the radial functions $u_\nu^\pm$ is negligible. Therefore, a viable approximation is obtained by the following steps:

1. Solve the radial model (9),
2. using the solutions thus obtained as an input in (19), solve for the concentrations under the electrode.

Hence, the solver of the equation (19),

$$F\colon (u_\nu^\pm(R, \cdot))_{\nu=1}^N \mapsto (\overline{u}_\nu^0(\cdot))_{\nu=1}^N, \tag{24}$$

can be viewed as an electrode correction, or a *gain function* for the inclusion of the device in the radial

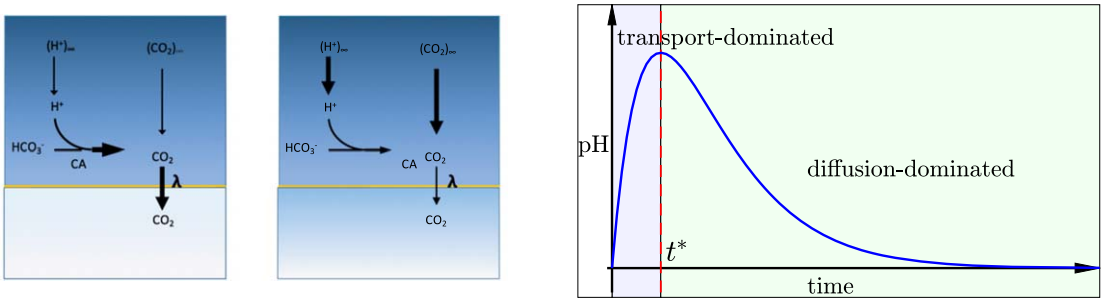

Figure 3. Left: When the concentration gradient of CO_2 across the membrane is high, the gas transport into the membrane induces a strong conversion flux of bicarbonate to CO_2, causing an increase of surface pH (transport-dominated phase). Center: At some time $t = t^*$, the gradient has decreased enough so that as the conversion of bicarbonate to CO_2 and thus the depletion of H^+ slows down, and the diffusion of H^+ from the unlimited equilibrium pool at infinity starts to dominate, causing the pH to drop towards the original equilibrium value.

model. In this manner, the algorithm separates the electrode effect into a separate step in the process, and it is easy to test the effect of the electrode-dependent parameters γ and h. This observation can be used effectively if several exchangeable measurements with the same oocyte are performed.

3. Analysis of the model

From the point of view of practical applicability of the model to estimate the membrane properties as well as the CA activity inside the cell and on the cell membrane, it is important to understand the effect of the parameters on the model predictions, as well as to test how the lumped model compares with the finite element model of [10]. The analysis presented in this section focusses on the following four parameters: the cell membrane permeability λ, the quench factor γ, and the carbonic anhydrase enhancement factor A inside and on the cell membrane, together with the enhancement A^0 in the electrode tip minicompartment. All other parameters will be held fixed at their default values.

We start with a short summary of the computed experiments on which the analysis is based, with a qualitative explanation of the expected outcomes of the pH simulations. For simplicity, the non-bicarbonate buffer is ignored in the discussion. At the beginning of the experiment, a strong gradient of CO_2 concentration across the membrane leads to significant depletion of CO_2 near the cell membrane outside of the cell, causing the association of H^+ with bicarbonate, and concomitant increase of surface pH. This phase is referred to as *transport-dominated phase*. As the across membrane gradient of the CO_2 concentration decreases, so does the transport flux across the membrane, and the H^+ concentration starts to increase again fueled by the diffusion from the unlimited equilibrium pool at infinity. Consequently, the surface pH starts to decrease again, eventually approaching the original equilibrium value. We refer to this phase as *diffusion-dominated phase*. The switch from the first to the second occurs at the time t^* when the surface pH reaches its peak value, see figure 3. Figure 4 shows the computed CO_2 profiles at the beginning of the experiment, at the time $t = t^*$ and at a significantly later time towards the final equilibrium. The decrease of the concentration gradient across the membrane is clearly visible in these profiles.

Next we examine the effect of each of the parameters of interest through a series of computed experiments. Throughout the experiments, the geometric constants are given in table 1, and the reaction rate constants in table 4. The initial values for the experiment are listed in table 3, and the diffusion coefficients in table 2. All values are the same as in [7], where the literature reference for each value is given.

Measured data and parameter range of CA activity: In [13], experimental data of the surface pH measured on Xenopus oocytes are reported. In the cited articles, the main interest is to analyze the role of the aquaporin gas channels on the membrane permeability for CO_2, and therefore, surface pH measurements are performed using oocytes that express the aquaporins and CA, and for comparison, oocytes expressing CA only. For details of the treatment of the oocytes and the experiment, we refer to the cited articles. In the experiments, it was found that the increase in surface pH is of order $\Delta pH_S \approx 0.13$ for water injected oocytes, and $\Delta pH_S \approx 0.25$ for oocytes expressing aquaporins, resulting in peak pH values $pH_S \approx 7.63$ and $pH_S \approx 7.75$, respectively. It is known [14] that the CA activity has a strong effect on the peak surface pH value, and that the observed peak values can be reached in simulations by increasing the value of the CA enhancement factor A by orders of magnitude. While the CA activity is believed to reach values of the order of magnitude $A = 10\,000$ and beyond, e.g., in erythrocytes [15], in our discussion below, we limit the CA enhancement to moderate values, $A \leqslant 50$. The motivation here is twofold: First, we show that observed peak values can be explained by the

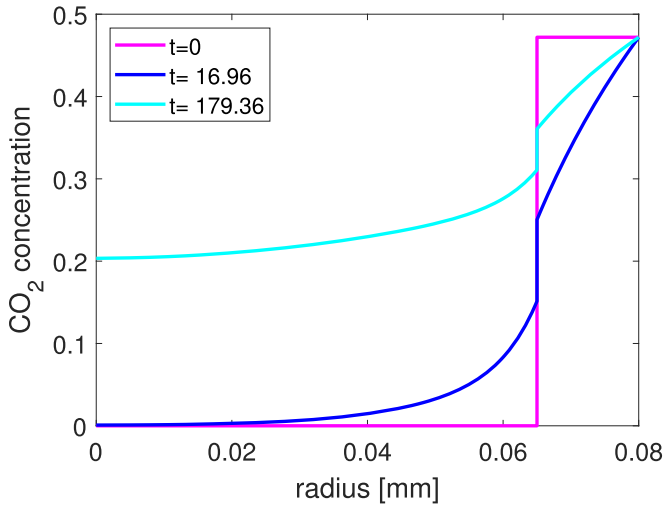

Figure 4. Three snapshots of the CO_2 profiles during the experiment. At $t = 0$, the concentrations inside and outside the cell are constants, and the concentration gradient decreases as a result of the transport of CO_2 through the membrane, converging to a constant concentration throughout the domain.

Table 1. Geometric parameters and membrane permeability corresponding to non-resistant membrane hypothesis.

R	Oocyte radius	650 μm
R_∞	External radius	800 μm
w	Radius of the electrode tip	10 μm
λ	Membrane permeability	34.2 μm/s

Table 2. Diffusion coefficients κ of the substances.

Substance	Inside [$(\mu$ m$)^2/s$]	Outside [$(\mu$ m$)^2/s$]
CO_2	1.71×10^3	1.71×10^3
H_2CO_3	1.11×10^3	1.11×10^3
HCO_3^-	1.11×10^3	1.11×10^3
H^+	8.69×10^3	8.69×10^3
HA	1.56×10^3	1.56×10^3
A^-	1.56×10^3	1.56×10^3

Table 3. Initial values of the concentrations in the standard experiment. The model assumes that at $t = 0$, the oocyte is added to the bath with the pH electrode already in place.

Substance	Inside [mM]	Outside [mM]
CO_2	0	0.4720
H_2CO_3	0	0.0013
HCO_3^-	0	9.901
H^+ (pH)	6.310×10^{-5} (7.2)	3.162×10^{-5} (7.5)
HA	12.09	2.500
A^-	15.22	2.500

introduction of the electrode tip model without increasing significantly the CA activity, and second, the model predictions are directly comparable with the earlier simulations in [7] where the same variable range was used.

Experiment 1: To set the reference, and to better understand the effect of each parameter in the electrode model, we start by running the one-dimensional radial model without the presence of the electrode, varying the membrane permeability only. In all experiments, the spatial discretization is refined near the membrane, the discretization points in the exterior domain being defined as

$$r_1 = R = 650\ \mu\text{m}, \quad r_j = r_{j-1} + \tau^{j-2}\Delta r, \quad j = 2, 3, \ldots, n^+,$$

where $\Delta r = 0.1\,\mu$m is the length of the first discretization interval near the membrane, and $\tau = 1.01$ is a coarsening factor that increases as one moves away from the membrane. The last discretization point is set equal the outer radius of the computational domain, $R_\infty = 800\ \mu$m, that is, we assume that the oocyte is surrounded by a layer of thickness of 150 μm of diffusive unstirred layer, outside which the concentrations are kept at the constant equilibrium values. The effect of the thickness of the unstirred layer was analyzed in [7], and will not be discussed further here. Similarly, we discretize the interior domain,

$$r'_{n-} = 650\ \mu\text{m}, \quad r'_j = r'_{j+1} - \tau^{n^- - j}\Delta r, \quad j = (n^- - 1), (n^- - 2), (n^- - 3), \ldots, 1,$$

the last point r'_1 being rounded to zero. With this discretization, we have $n^+ = 88$, $n^- = 118$, and the number of unknown concentration values $n = 205$, as at the outmost point the value is given.

We run the free membrane radial model, assuming that the carbonic anhydrase enhancement factor inside the cell and at the outer surface of the membrane is $A = 20$. In the first experiment, we compute the surface pH curve over the time interval $[0, T]$, $T = 1200$ s, letting the membrane permeability take on the values

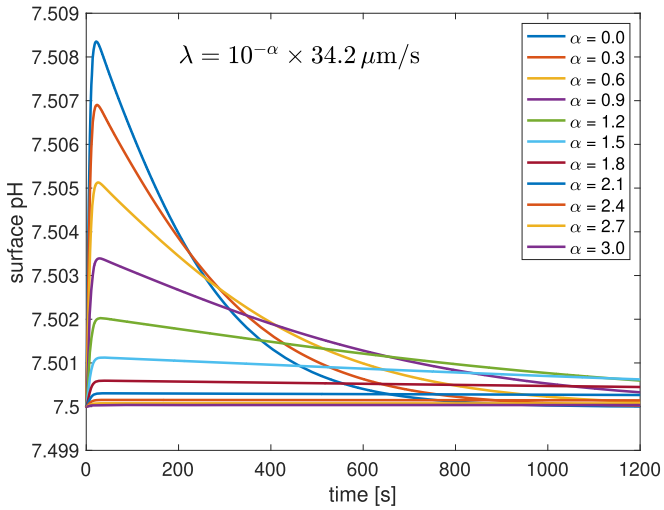

Figure 5. Surface pH on the exterior of free cell membrane (no electrode included) with varying membrane permeabilities.

Table 4. Reaction rates. Observe that we have two fast time scale parameters, ε and ε', whose precise values in the fast/slow propagation scheme used in [3] are not important, since only the ratios defining the equilibrium conditions are needed in the model. When carbonic anhydrase is present, the reaction rates $k_{\pm 1}$ are enhanced by an acceleration factor, denoted by A.

Reaction	k_ℓ	$k_{-\ell}$	$K = k_\ell / k_{-\ell}$
$CO_2 + H_2O \rightleftharpoons^{k_1}_{k_{-1}} H_2CO_3$	0.0302 [1/s]	10.9631 [1/s]	2.7547×10^{-4}
$H_2CO_3 \rightleftharpoons^{k_2}_{k_{-2}} HCO_3^- + H^+$	$\varepsilon = 10^{-9}$ [1/s]	ε / K_2	$K_2 = 0.2407$ [mM]
$HA_{in} \rightleftharpoons^{k_3}_{k_{-3}} A^-_{in} + H^+_{in}$	$\varepsilon' = 10^{-6}$ [1/s]	ε' / K_{HA}	$K_{HA} = 7.9433 \times 10^{-5}$ [mM]
$HA_{out} \rightleftharpoons^{k_3}_{k_{-3}} A^-_{out} + H^+_{out}$	$\varepsilon' = 10^{-6}$ [1/s]	ε' / K_{HA}	$K_{HA} = 3.1623 \times 10^{-5}$ [mM]

$$\lambda_j = 10^{-\alpha_j} \times 34.2\ \mu\text{m/s}, \quad \alpha_j = j \times 0.3,$$
$$j = 0,\ 1,\ldots,10,$$

where the baseline value λ_0 is based on the hypothesis of non-resistive membrane layer. The results are shown in figure 5.

As λ decreases, so does the CO_2 flux across the membrane, reducing the depletion rate of H^+ during the transport-dominated phase. Consequently, the peak surface pH becomes lower, approaching asymptotically the original equilibrium value as $\lambda \to 0+$. Moreover, as λ decreases, it takes increasingly longer time to reach the equilibrium where the CO_2 concentration inside and outside of the cell are equal, flattening the pH curve in the diffusion-dominated phase. This causes an increase of the *half width* of the pH curve, defined as the time that it takes to reduce the pH increase to half of its value,

$$HW = t_{1/2} - t^*,$$

where

$$\begin{aligned} t^* &= \text{argmax}\{\text{pH}_S(t)\}, \quad t_{1/2} \\ &= \min\{t > t^* | \text{pH}_S(t) - \text{pH}_S(0) \\ &\leqslant 0.5(\text{pH}_S(t^*) - \text{pH}_S(0))\}. \end{aligned}$$

We conclude that the predictions of the current FEM model agree with those of the finite difference model in [7]. According to the model, moderate CA activity values are not sufficient to produce the observed increase in surface pH, the maximum increase being only approximately 3%–6% of the measured increases.

Experiment 2: In this experiment, we introduce the electron tip microenvironment, solving the same problem as is Experiment 1 with the addition of the electrode compartment, and we assume no carbonic anhydrase activity under the electrode tip, which is achieved by setting $A^0 = 1$ in (20), while assuming that the CA enhancement factor on the membrane and inside the cell in the radial model is $A = 20$. The assumption of no CA activity under the electrode is unrealistic because of the presence of the cell membrane, but the purpose of this experiment is to test if the model predictions are in line with what is expected.

We run the lumped electrode model with the same discretization, and reductions of the membrane permeability as in the previous experiment, using two different values for the quench factor,

$$\gamma_1 = 10\ \mu\text{m/s}, \quad \gamma_2 = 1\ \mu\text{m/s}.$$

The results are shown in figure 6. We observe that when the value of γ is decreased, the diffusion from the equilibrium pool to the minicompartment becomes weaker. Consequently, the transport of CO_2 becomes

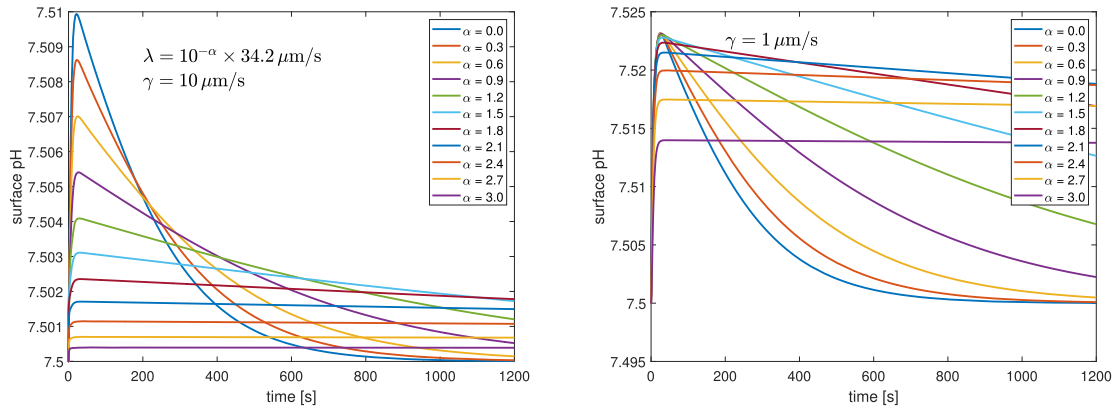

Figure 6. Surface pH on the exterior of cell membrane under the electrode tip for different values of the membrane permeability, and two values of the quench factor γ. In this computer experiment, there is no CA enhancement in the minicompartment under the electrode tip.

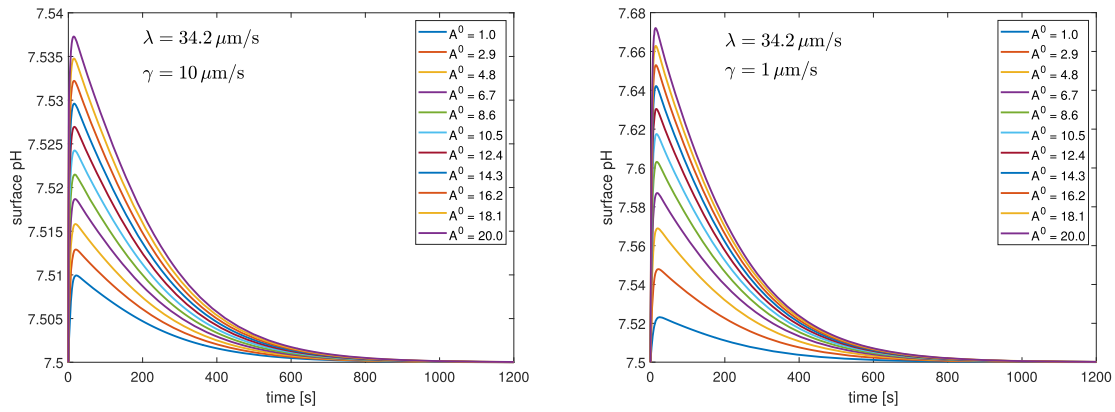

Figure 7. Surface pH on the exterior of the cell membrane under the electrode tip with varying carbonic anhydrase activity in the electrode compartment corresponding to two different values of the quench parameter γ.

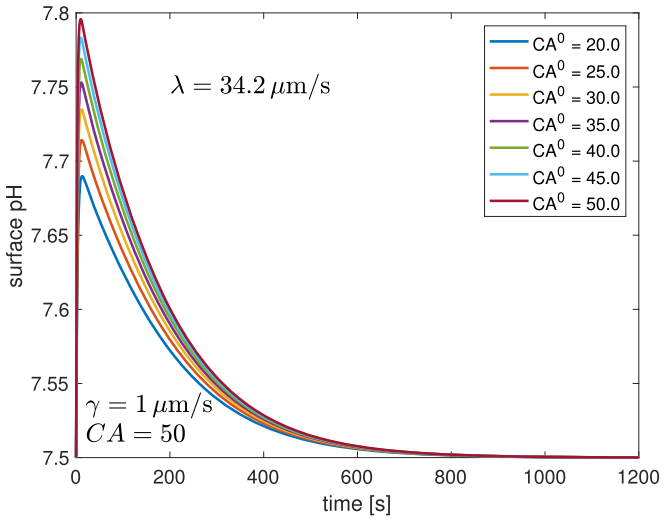

Figure 8. Surface pH under the electrode with different values of the CA activity under the electrode.

more dominant, leading to a higher peak value of the surface pH. Moreover, with decreasing diffusion from the exterior domain into the compartment under the electrode where the pH is measured, the decrease of pH in the diffusion-dominated phase becomes slower, leading to a significant increase in the half width.

Summarizing, we observe that by introducing the microenvironment, the surface pH peak value

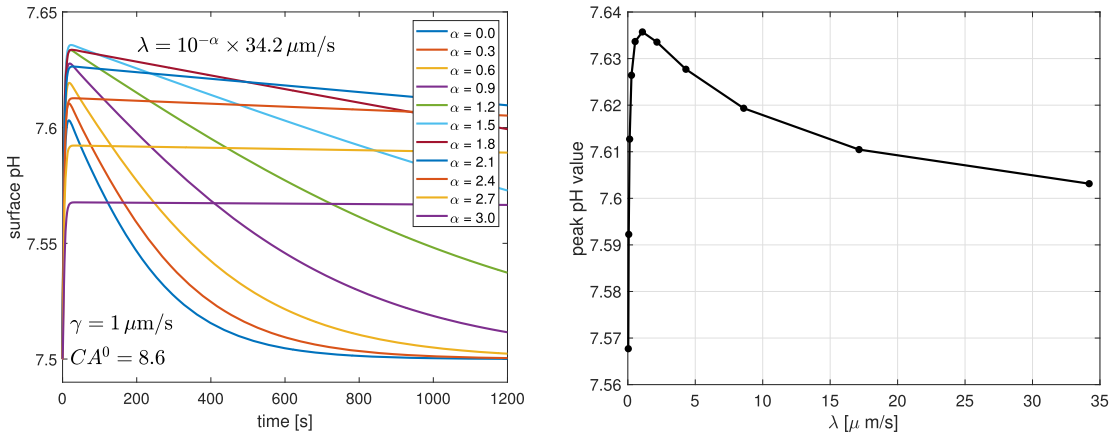

Figure 9. Left: Surface pH on the exterior of the cell membrane under the electrode tip with varying membrane permeability. Right: The peak surface pH as a function of λ.

increases from the value obtained without the electrode, however, without introducing the CA enhancement under the electrode tip, the maximum pH increase remains at 4%–8% of the measured values with $\gamma = 10\ \mu$ m/s, and 9%–18% with $\gamma = 1\ \mu$ m/s. The conclusion is that the CA enhancement under the electrode is necessary to obtain realistic values.

Experiment 3: In the previous experiment, we assumed that the CA was not present in the electrode compartment, while it was assumed to affect the reactions inside the cell as well as at the free membrane. The absence of CA in the electrode tip compartment is likely to make the conversion of bicarbonate to CO_2 unrealistically slow, affecting in particular the transport-dominated phase. We expect that if carbonic anhydrase is included in the compartment, the pH peak value will be significantly higher.

To test this hypothesis, we fix the membrane permeability to the default value of $\lambda = 34.4\ \mu$m/s, and vary the CA enhancement coefficient A^0 from $A^0 = 1$ up to the value assumed inside the cell, $A^0 = 20$. We run this experiment with two different values of the quench factor, $\gamma = 10\ \mu$m/s and $\gamma = 1\ \mu$m/s. The results are shown in figure 7. As expected, the peak value of the surface pH increases with increasing CA activity. Moreover, the growth is more significant when the quench factor is smaller, limiting more the diffusion process that feeds the conversion of bicarbonate to carbonic acid and further to carbon dioxide.

The increase of the surface pH at the peak is 0.038 with $\gamma = 10\ \mu$ m/s, amounting to 15%–29% of the observed increase. With $\gamma = 1\ \mu$ m/s, the increase is 0.17, enough to explain the measured increase in the absence of the aquaporins, and arriving at 68% of the peak value in the presence of the aquaporins.

Experiment 4: The previous experiment demonstrated that the introduction of the microenvironment under the electrode combined with moderate CA activity can explain the surface pH peak value in the absence of aquaporins. The current experiment shows that only a slight increase in the CA activity, in fact, suffices to cover the dynamical range of the experiment with aquaporin-injected oocyte. In this experiment, we increase the CA-induced enhancement to $A = 50$ inside the cell and on the membrane, and let the enhancement factor A^0 under the electrode vary from 20 to 50. The quenching parameter is fixed at $\gamma = 1\ \mu$ m/s. The surface pH curves are shown in figure 8. The simulation shows that the model can reproduce the dynamical range of the measured peak values without increasing disproportionally the CA activity enhancement.

Experiment 5: The previous experiments illustrated how the different parameters affect the surface pH, which may be useful for the design of a strategy for estimating the model parameters from measured data. While the effect of varying one parameter at the time is fairly straightforward to understand, the joint effect of changing several parameters at once may not be easily predictable, as there may be effects that partially cancel each other. To elucidate this point, we run an experiment in which the membrane permeability is reduced as in Experiments 1 and 2, but this time in the presence of the electrode and with carbonic anhydrase in the minicompartment. Observe that while in the case of free membrane, the effect of reducing the membrane permeability is predictable as explained in Experiment 1, in the presence of the electrode, the situation is more complex as the membrane permeability appears also in the auxiliary equation (19), and therefore affects the gain functional as well. In the following example, the quench factor is fixed at value $\gamma = 1\ \mu$m/s, the carbonic anhydrase activity in the minicompartment is set to $A^0 = 8.6$, while the membrane permeability is reduced by a multiplicative factor as in Experiments 1 and 2 from the non-resistive value. The results in figure 9 show that while the half width of the pH curve increases monotonically as in the free membrane case, the peak pH value is no longer monotonic as a function of the permeability reduction. Starting from the non-reduced value $\lambda = 34.2\ \mu$ m/s and reducing the permeability by the factor $10^{-\alpha}$ as indicated in the figure, the peak pH increases up to value $\lambda = 1.08\ \mu$ m/s , after which it starts to decrease, reaching the smallest

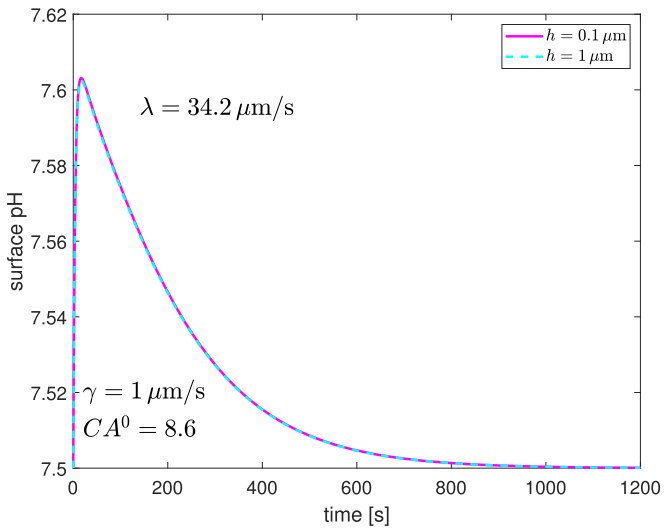

Figure 10. The surface pH curve computed with two different values of the electrode tip distance from the membrane, $h = 1\ \mu$m and $h = 0.1\ \mu$m. The other model parameters are indicated in the figure.

value $\lambda = 0.034\ \mu$ m/s at $\alpha = 3$ in this simulation. The effect of varying λ in the presence of the electrode is primarily not due to the term in (19) depending on the ratio λ/h, since numerical simulations reveal that varying h has a minimal effect on the output. To verify the latter statement, consider figure 10 in which we compute the pH curve by varying h across an order of magnitude, between $h = 0.1\ \mu$m and $h = 1\ \mu$m. The curves are almost perfectly overlaying, only the peak value changes slightly. Observe that making h significantly greater than $h = 1\ \mu$m is not meaningful for the present model, since we are assuming that the sensor measures the pH right above the surface of the cell, which means that it should be very close to the surface, that is, h is the scale of μm which is one tenth of the diameter of the electrode tip.

4. Discussion and conclusions

This article introduces a reduced complexity model for following the dynamics of the pH inside and on the outer membrane of an oocyte under the assumptions that the pH dynamics arises from the transport of carbon dioxide through the cell membrane driven by a concentration gradient across the membrane. The proposed model is based on the further assumption that the transport of acids (H^+) and bases (HCO_3^-) is negligible, and assumes that the gas transport is described by Fick's law. The model takes into account the effects of the presence of the pH electrode itself, which is hypothesized to be the explaining factor of the discrepancy between the pH predictions of the radial free membrane model and the measured values. Numerical evidence using a detailed finite element discretization supports this hypothesis, however, at the moment a tool for estimating properties of the membrane from the surface pH data is still missing. Computer experiments presented in this article indicate that the proposed model can produce plausible pH time traces, with a dynamical range covering well the measured pH values even with moderate enhancement by the carbonic anhydrase activity. The next natural step in the study of cross membrane gas transport is to develop efficient numerical methods for estimating the model parameters from the measured data, an endeavor that will be pursued in a forthcoming article.

Acknowledgments

The work of DC was partially supported by the NSF-DMS grant 1 951 446.

Data availability statement

No new data were created or analysed in this study.

Appendix A

In this appendix we present some of the computational details. The mass balance equations for a system that does not include the enzyme carbonic anhydrase, are of the form

$$\begin{aligned}
&CO_2 + H_2O \xrightarrow{k_1} H_2CO_3, \quad \Phi_1 = k_1 u_1,\\
&H_2CO_3 \xrightarrow{k_{-1}} CO_2 + H_2O, \quad \Phi_2 = k_{-1} u_2,\\
&H_2CO_3 \xrightarrow{k_2} HCO_3^- + H^+, \quad \Phi_3 = k_2 u_2,\\
&H^+ + HCO_3^- \xrightarrow{k_{-2}} CO_2 + H_2CO_3, \quad \Phi_4 = k_{-2} u_3 u_4,\\
&HA \xrightarrow{k_3} A^- + H^+, \quad \Phi_5 = k_3 u_5,\\
&H^+ + A^- \xrightarrow{k_{-3}} HA, \quad \Phi_6 = k_{-3} u_6 u_4.
\end{aligned} \tag{25}$$

Carbonic anhydrase is accounted for by speeding up the fluxes of the reactions involving carbon dioxide up by a factor $A > 1$, thus replacing $k_{\pm 1}$ by $Ak_{\pm 1}$. The stoichiometric matrix $\mathsf{S} \in \mathbb{R}^{6\times 6}$ for the system is

$$\mathsf{S} = \begin{bmatrix} -1 & 1 & 0 & 0 & 0 & 0 \\ 1 & -1 & 0 & 0 & 0 & 0 \\ 0 & -1 & 1 & 1 & 0 & 0 \\ 0 & 1 & -1 & -1 & 0 & 0 \\ 0 & 0 & 0 & 1 & -1 & 1 \\ 0 & 0 & 0 & -1 & 1 & -1 \end{bmatrix}.$$

Appendix B

In this appendix we present some details of the radial finite element model (9).

Consider first the exterior domain $r > R$. We truncate the domain at some value $R_\infty > R$, and assume that the Dirichlet data at $r = R_\infty$ are given,

$$u_\nu^+(R_\infty, t) = u_{\nu,0}^+, \quad 1 \leqslant \nu \leqslant N. \tag{26}$$

We discretize the spatial part using the Galerkin approximation with second order piecewise polynomial basis functions. To this end, we divide the interval $[R, R_\infty]$ in K intervals, or elements, denoted by T_k, and add to each interval an additional node. In this manner, we obtain the nodes

$$r_1 = R < r_2 < \ldots < r_{n^+} = R_\infty, \quad n^+ = 2K + 1,$$

where $T_k = [r_{2k-1}, r_{2k+1}]$, $1 \leqslant k \leqslant K$. We define three second order shape functions over $[0, 1]$,

$$\begin{aligned} \varphi_1(t) &= 2(t - 1/2)(t - 1), \\ \varphi_2(t) &= 4t(1 - t), \\ \varphi_3(t) &= 2t(t - 1/2). \end{aligned}$$

For a given element T_k, we define

$$F_k\colon [0, 1] \to T_k, \quad F(t) = (1 - t)r_{2k-1} + r_{2k+1}t = r,$$

and subsequently we define the three non-vanishing basis functions over T_k,

$$\psi_{2k-2+\ell}(r) = \varphi_\ell(F_k^{-1}(r)), \quad 1 \leqslant \ell \leqslant 3.$$

The basis functions, defined elementwise, constitute a second order Lagrange basis, satisfying the condition

$$\psi_p(r_q) = \delta_{pq}, \quad 1 \leqslant p, q \leqslant n^+,$$

where δ_{pq} is the Kronecker symbol.

We multiply the reaction-diffusion equation (5) above the membrane by $r^2\psi_p(r)$, $1 \leqslant p < n^+$, and integrate over the interval $[R, R_\infty]$, to get

$$\begin{aligned} &\frac{\partial}{\partial t}\int_R^{R_\infty} \psi_p(r)u_\nu^+(r, t)r^2dr \\ &= \int_R^{R_\infty} \psi_p(r)\frac{\partial}{\partial r}\left(\kappa_\nu^+ r^2\frac{\partial u_\nu^+}{\partial r}\right)dr \\ &\quad + \sum_{\mu=1}^N S_{\nu\mu}\int_R^{R_\infty} \psi_p(r)\Phi_\mu^+(r, t)r^2dr. \end{aligned} \tag{27}$$

Integrating by parts, the first term of the expression on the right assumes the form

$$\begin{aligned} &\int_R^{R_\infty} \psi_p\frac{\partial}{\partial r}\left(\kappa_\nu^+ r^2\frac{\partial u_\nu^+}{\partial r}\right)dr \\ &= \psi_p(R_\infty)\kappa_\nu^+ R_\infty^2\frac{\partial u_\nu^+}{\partial r}(R_\infty) \\ &\quad - \psi_p(R)\kappa_\nu^+ R^2\frac{\partial u_\nu^+}{\partial r}(R) \\ &\quad - \int_R^{R_\infty} \frac{d\psi_p}{dr}\left(\kappa_\nu^+ r^2\frac{\partial u_\nu^+}{\partial r}\right)dr \\ &= -\delta_{p1}\kappa_\nu^+ R^2\frac{\partial u_\nu^+}{\partial r}(R) \\ &\quad - \int_R^{R_\infty} \frac{d\psi_p}{dr}\left(\kappa_\nu^+ r^2\frac{\partial u_\nu^+}{\partial r}\right)dr, \end{aligned}$$

where we used the fact that $\psi_p(R_\infty) = \psi_p(r_{n^+}) = 0$ for $p < n^+$. It follows from the conditions (6) on the membrane boundary that

$$\begin{aligned} &\int_R^{R_\infty} \psi_p\frac{\partial}{\partial r}\left(\kappa_\nu^+ r^2\frac{\partial u_\nu^+}{\partial r}\right)dr \\ &= -\delta_{\nu 1}\delta_{p1}R^2\lambda(u_\nu^+(R, t) - u_\nu^-(R, t)) \\ &\quad - \int_R^{R_\infty} \frac{d\psi_p}{dr}\left(\kappa_\nu^+ r^2\frac{\partial u_\nu^+}{\partial r}\right)dr. \end{aligned}$$

To discretize the problem, we write the approximation

$$u_\nu^+(r, t) = \sum_{q=1}^{n^+} U_{q\nu}^+(t)\psi_q(r), \tag{28}$$

where $U_{q\nu}^+(t) = u_\nu^+(r_q, t)$. At $r = r_n^+ = R_\infty$, we assume a constant Dirichlet condition,

$$U_{n^+\nu}^+(t) = u_\nu^\infty,$$

where the concentrations u_ν^∞ satisfy an equilibrium condition. In particular, the time derivative at the boundary vanishes, and the left hand side of (27) becomes

$$\frac{\partial}{\partial t}\int_R^{R_\infty} \psi_p(r)u_\nu^+(r, t)r^2dr = \sum_{q=1}^{n^+-1} M_{pq}^+\frac{dU_{q\nu}^+}{dt}$$

where M^+ is the mass matrix with entries

$$M_{pq}^+ = \int_R^{R_\infty} \psi_p\psi_q r^2dr, \quad 1 \leqslant p < n^+, 1 \leqslant q < n^+ \tag{29}$$

Consider now the stiffness integral on the right hand side of (27). Substituting the approximation (28), we obtain

$$\begin{aligned} &\int_R^{R_\infty} \frac{\partial\psi_p}{\partial r}\left(\kappa_\nu^+ r^2\frac{\partial u_\nu^+}{\partial r}\right)dr \\ &= \textstyle\sum_{q=1}^{n^+-1} \mathsf{K}_{\nu,pq}^+ U_{q\nu}^+ + W_{p\nu}u_\nu^\infty, \end{aligned} \tag{30}$$

where the stiffness matrix K_ν^+ has the entries

$$\mathsf{K}_{\nu,pq}^+ = \int_R^{R_\infty} \kappa_\nu^+\frac{d\psi_p}{dr}\frac{d\psi_q}{dr}r^2dr, \quad 1 \leqslant p, q < n^+, \tag{31}$$

and

$$W_{p,\nu} = \int_R^{R_\infty} \kappa_\nu^+ \frac{d\psi_q}{dr}\frac{d\psi_{n^+}}{dr} r^2 dr, \quad 1 \leqslant p < n^+. \tag{32}$$

Finally, we approximate the reaction terms by

$$\Phi_\mu^+(r,\, t) = \sum_{q=0}^{n^+} \Phi_{q\mu}^+(t)\psi_q(r) = \sum_{q=0}^{n^+-1} \Phi_{q\mu}^+(t)\psi_q(r),$$

where we used the fact that the fluxes vanish at R_∞ because of the assumed equilibrium. The reaction term in the equation then becomes

$$\begin{aligned}
&\sum_{\mu=1}^{N} S_{\nu\mu} \int_R^{R_\infty} \psi_p(r)\Phi_\mu^+(r,\, t) r^2 dr \\
&\quad = \sum_{\mu=1}^{N} S_{\nu\mu} \sum_{q=1}^{n^+-1} \Phi_{q\mu}^+ \int_R^{R_\infty} \psi_p \psi_q r^2 dr \\
&\quad = \sum_{\mu=1}^{N} S_{\nu\mu} \sum_{q=1}^{n^+-1} M_{pq}^+ \Phi_{q\mu}^+.
\end{aligned}$$

Before vectorizing the equation, consider the reaction-diffusion equation inside the cell. This time, the discretization points are

$$r_1' = 0 < r_2' < \ldots < r_{n^-}' = R,$$

and we define the second order basis functions as in the exterior domain. With a slight abuse of notations, we denote the basis functions by ψ_j as in the exterior domain. Multiplying the reaction-diffusion equation by $r^2\psi_p$ and integrating over $[0, R]$, we obtain

$$\begin{aligned}
&\frac{\partial}{\partial t}\int_0^R \psi_p(r) u_\nu^-(r,\, t) r^2 dr \\
&\quad = \int_0^R \psi_p(r)\frac{\partial}{\partial r}\left(\kappa_\nu^- r^2 \frac{\partial u_\nu^-}{\partial r}\right) dr \\
&\qquad + \sum_{\mu=1}^{N} S_{\nu\mu} \int_0^R \psi_p(r)\Phi_\mu^-(r,\, t) r^2 dr, \\
&\quad 1 \leqslant p \leqslant n^-.
\end{aligned} \tag{33}$$

As before, integrating by parts the first term on the right, and using the condition that the radial derivative of u^- at $r = 0$ must be finite,

$$\begin{aligned}
&\int_0^R \psi_p \frac{\partial}{\partial r}\left(\kappa_\nu^- r^2 \frac{\partial u_\nu^-}{\partial r}\right) dr \\
&\quad = \psi_p(R)\kappa_\nu^- R^2 \frac{\partial u_\nu^-}{\partial r}(R) \\
&\qquad - \int_0^R \frac{d\psi_p}{dr}\left(\kappa_\nu^- r^2 \frac{\partial u_\nu^-}{\partial r}\right) dr \\
&= \delta_{p,n^-}\kappa_\nu^- R^2 \frac{\partial u_\nu^-}{\partial r}(R) - \int_0^R \frac{d\psi_p}{dr}\left(\kappa_\nu^- r^2 \frac{\partial u_\nu^-}{\partial r}\right) dr \\
&\quad = \delta_{\nu 1}\delta_{p,n^-} R^2 \lambda (u_\nu^+(R,\, t) - u_\nu^-(R,\, t)) \\
&\qquad - \int_0^R \frac{d\psi_p}{dr}\left(\kappa_\nu^- r^2 \frac{\partial u_\nu^-}{\partial r}\right) dr.
\end{aligned}$$

We may now define the mass and stiffness matrices $\mathsf{M}^- \in \mathbb{R}^{n^-\times n^-}$ and $\mathsf{K}^- \in \mathbb{R}^{n^-\times n^-}$ as in the exterior domain. To glue the interior and exterior solutions together by the boundary condition at the membrane boundary, we define

$$\begin{aligned}
U_\nu = \begin{bmatrix} U_\nu^- \\ U_\nu^+ \end{bmatrix} \in \mathbb{R}^n, \;\; \Phi_\nu = \begin{bmatrix} \Phi_\nu^- \\ \Phi_\nu^+ \end{bmatrix} \in \mathbb{R}^n, \\
n = n^- + n^+ - 1,
\end{aligned} \tag{34}$$

combine the mass and stiffness matrices as

$$\mathsf{M} = \begin{bmatrix} \mathsf{M}^- & \mathsf{O} \\ \mathsf{O} & \mathsf{M}^+ \end{bmatrix} \in \mathbb{R}^{n\times n}, \;\; \mathsf{K}_\nu = \begin{bmatrix} \mathsf{K}_\nu^- & \mathsf{O} \\ \mathsf{O} & \mathsf{K}_\nu^+ \end{bmatrix} \in \mathbb{R}^{n\times n}, \tag{35}$$

and define

$$\mathsf{W}_\nu = \begin{bmatrix} 0 \\ W_\nu \end{bmatrix} \in \mathbb{R}^{n\times 1}, \tag{36}$$

where W_ν is a vector of length $n^+ - 1$ with entries given by (32). Furthermore, we define a coupling matrix $\mathsf{C} \in \mathbb{R}^{n\times n}$ that accounts for the gas transport with all zero entries except for four of them, which are

$$\begin{aligned}
\mathsf{C}_{n^-,n^-} &= \mathsf{C}_{n^-+1,n^-+1} = -R^2, \\
\mathsf{C}_{n^-,n^-+1} &= \mathsf{C}_{n^-+1,n^-} = R^2.
\end{aligned} \tag{37}$$

and ,we define the matrix

$$\Phi = [\Phi_1 \;\; \cdots \;\; \Phi_N] \in \mathbb{R}^{n\times N}. \tag{38}$$

With these notations, the Galerkin approximation of the reaction-diffusion equations assumes the form

$$\begin{aligned}
\mathsf{M}\frac{dU_\nu}{dt} &= -\mathsf{K}_\nu U_\nu + \lambda\delta_{\nu,1}\mathsf{C}U_\nu + \mathsf{W}_\nu u_\nu^\infty \\
&\quad + \mathsf{M}(\Phi\mathsf{S}^\mathsf{T})_\nu, \quad 1 \leqslant \nu \leqslant N.
\end{aligned} \tag{39}$$

To complete the vectorization, we stack all the vectors U_ν into a large vector,

$$\mathbf{U} = \begin{bmatrix} U_1 \\ \vdots \\ U_N \end{bmatrix} \in \mathbb{R}^{Nn}, \tag{40}$$

and define the block diagonal matrices

$$\begin{aligned}
\mathscr{M} &= \begin{bmatrix} \mathsf{M} & & \\ & \ddots & \\ & & \mathsf{M} \end{bmatrix} \in \mathbb{R}^{nN\times nN}, \\
\mathscr{K} &= \begin{bmatrix} \mathsf{K}_1 & & \\ & \ddots & \\ & & \mathsf{K}_N \end{bmatrix} \in \mathbb{R}^{nN\times nN},
\end{aligned} \tag{41}$$

and

$$\begin{aligned}
\mathscr{W} &= \begin{bmatrix} \mathsf{W}_1 & & \\ & \ddots & \\ & & \mathsf{W}_N \end{bmatrix} \in \mathbb{R}^{Nn\times N}, \\
\mathscr{C} &= \begin{bmatrix} \mathsf{C} & & \\ & \ddots & \\ & & \mathsf{O} \end{bmatrix} \in \mathbb{R}^{nN\times nN}.
\end{aligned}$$

This allows us to write the full system as

$$\mathscr{M}\frac{d\mathbf{U}}{dt} = -\mathscr{K}\mathbf{U} + \lambda\mathscr{C}\mathbf{U} + \mathscr{W}\mathbf{U}^\infty + \mathrm{vec}(\mathsf{M}\Phi\mathsf{S}^\mathsf{T}), \tag{42}$$

where vec: $\mathbb{R}^{n\times N} \to \mathbb{R}^{nN}$ is the operation of stacking columns of a matrix into a single vector, and $\mathbf{U}^\infty \in \mathbb{R}^N$ is the boundary value vector containing the equilibrium values at the outer boundary.

The ODE system obtained in this manner is stiff, but can be solved by using built-in stiff numerical time integrators.

ORCID iDs

A Bocchinfuso https://orcid.org/0000-0002-6063-4131
D Calvetti https://orcid.org/0000-0001-5696-718X
E Somersalo https://orcid.org/0000-0001-5099-3512

References

[1] Overton E 1895 Über die osmotischen Eigenschaften der Zelle in ihrer Bedeutung für die Toxikologie und Pharmacologie *Z Phys Chem* **22** 189–209
[2] Waisbren S J, Geibel J P, Modlin I M and Boron W F 1994 Unusual permeability properties of gastric gland cells *Nature* **368** 332–5
[3] Boron W F 2010 The Sharpey-Schafer lecture: Gas channels *Exp Physiol* **95** 1107–30
[4] Michenkova M *et al* 2021 Carbon dioxide transport across membranes *Interface Focus* **11** 20200090
[5] Nakhoul N L, Davis B A, Romero M F and Boron W F 1998 Effect of expressing the water channel aquaporin-1 on the CO_2 permeability of Xenopus oocytes *Am J Physiol* **274** C543–8
[6] Boron W F and DeWeer P 1976 Intracellular pH transients in squid giant axons caused by CO_2, NH_3 and metabolic inhibitors *J Gen Physiol* **67** 91–112
[7] Somersalo E, Occhipinti R, Boron W F and Calvetti D 2012 A reaction-diffusion model of CO_2 influx into an oocyte *J Theor Biol* **309** 185–203
[8] Musa-Aziz R, Chen L, Pelletier M F and Boron W F 2009 Relative CO_2/NH_3 selectivities of AQP1, AQP4, AQP5, AmtB, and RhAG *Proc Natl Acad Sci USA* **106** 5406–11
[9] Cooper G J and Boron W F 1997 The CO_2 permeability of the AQP1 water channel, expressed in Xenopus oocytes *J Am Soc Nephrol* **8** 16A
[10] Calvetti D, Prezioso J, Occhipinti R, Boron W F and Somersalo E 2020 Computational model for electron-induced micro-environmental effects on pH measurements near cell membrane *Multiscale Model Simul* **18** 1053–75
[11] Fei Y J, Kanai Y, Nussberger S, Ganapathy V, Leibach F H, Romero M F, Singh S K, Boron W F and Hediger M A 1994 Expression cloning of a mammalian proton-coupled oligopeptide transporter *Nature* **368** 563–6
[12] Costa P F, Emilio M G, Fernandes P L, Ferreira H G and Ferreira K G 1989 Determination of ionic permeability coefficients of the plasma membrane of Xenopus laevis oocytes under voltage clamp *J Physiol* **413** 199–211
[13] Endeward V, Musa-Aziz R, Cooper G J, Chen L, Pelletier M F, Virkki L V, Supuran C T, King L S, Boron W F and Gros G 2006 Evidence that aquaporin 1 is a major pathway for CO_2 transport across the human erythrocyte membrane *FASEB J* **20** 1974–81
[14] Occhipinti R and Boron W F 2019 Role of carbonic anhydrases and inhibitors in acid?base physiology: insights from mathematical modeling *Int. J. Mol. Sci.* **20** 3841
[15] Geers C and Gros G 2000 Carbon dioxide transport and carbonic anhydrase in blood and muscle *Physiol Rev* **80** 681–715
[16] Cooper G J, Occhipinti R and Boron W R 2015 CrossTalk proposal: Physiological CO_2 exchange can depend on membrane channels *J Physiol* **593** 5025–8
[17] Endeward V and Gros G 2005 Low carbon dioxide permeability of the apical epithelial membrane of guinea-pig colon *J Physiol* **567** 253–65
[18] Endeward V and Gros G 2009 Extra-and intracellular unstirred layer effects in measurements of CO_2 diffusion across membranes- a novel approach applied to the mass spectrometric ^{18}O technique for red blood cells *J Physiol* **587** 1153–67
[19] Gunshin H, Mackenzie B, Berger U V, Gunshin Y, Romero M F, Boron W F, Nussberger S, Gollan J L and Hediger M A 1997 Cloning and characterization of a mammalian proton-coupled metal-ion transporter *Nature* **388** 482–8
[20] Lee S-K, Boron W F and Parker M D 2011 Relief of autoinhibition of the electrogenic Na/HCO_3 cotransporter NBCe1-B: role of IRBIT versus amino-terminal truncation *Am J Physiol CellPhysiol* **302** C518–26
[21] Missner A, Kugler P, Saparov S M, Sommer K, Mathai J C, Zeidel M L and Pohl P 2008 Carbon dioxide transport through membranes *J Biol Chem* **283** 25340–7
[22] Musa-Aziz R, Occhipinti R and Boron W F 2014 Evidence from simultaneous intracellular and surface-pH transients that carbonic anhydrase IV enhances CO_2 fluxes across Xenopus oocyte plasma membranes *Am J Physiol-Cell Physiol* **307** C814–40
[23] Steel A, Nussberger S, Romero M F, Boron W F, Boyd C A R and Hediger M A 1997 Stoichiometry and pH-dependence of the mammalian proton-dependent oligopeptide transporter PepT1 *J. Physiol. (London)* **498** 563–9
[24] Toye A M, Parker M D, Daly C M, Lu J, Virkki L V, Pelletier M F and Boron W F 2006 The human NBCe1-A mutant R881C, associated with proximal renal tubular acidosis, retains function but is mistargeted in polarized renal epithelia *Am J Physiol -Cell Physiol* **291** C788–801
[25] Vaughan-Jones R D, Peercy B E, Keener J P and Spitzer K W 2002 Intrinsic H ion mobility in the rabbit ventricula rmyocyte *J Physiol* **541** 139–58